Energy & Environmental Science

PAPER

View Article Online
View Journal | View Issue

Cite this: *Energy Environ. Sci.*, 2014, **7**, 736

Use of potential determining ions to control energetics and photochemical charge transfer of a nanoscale water splitting photocatalyst†

Rachel L. Chamousis and Frank E. Osterloh*

Tetrabutylammonium (TBA) stabilized $H[Ca_2Nb_3O_{10}]$ nanosheets catalyze hydrogen evolution from aqueous methanol under illumination with UV light. Here we show that surface treatment with protons, potassium, and strontium potential-determining cations (PDIs) in aqueous solution modifies the electrostatic, energetic and photocatalytic properties of this nanomaterial. Attachment of cations to the nanocrystals was verified with elemental dispersive spectroscopy. Zeta potentials were measured as −40 mV (TBA+, pH = 4.8), −50 mV (K^+, pH = 4.3), and −20 mV (Sr^{2+}, pH = 4.4). Photoelectrochemical measurements in methanol containing 0.1 M tetraethylammonium chloride revealed anodic current photoonset potentials/Fermi energies ranging between −0.59 V (Sr^{2+}) and −0.71 V (at pH = 7, *vs.* NHE). The photocatalytic proton reduction ability of the modified nanocrystals was assessed in aqueous methanol at pH = 1. Here, $K_xH_{1-x}[Ca_2Nb_3O_{10}]$ evolved hydrogen at 350 μmol H_2 h^{-1}, $Sr_xH_{1-2x}[Ca_2Nb_3O_{10}]$ at 70 μmol H_2 h^{-1}, and $H[Ca_2Nb_3O_{10}]$ at 160 μmol H_2 h^{-1}. In addition, the photocatalytic activity was found to increase (20–160 μmol H_2 h^{-1}) with solution pH. These observed activity variations can be quantitatively understood using a linear free energy relationship between the proton reduction rate constant and the free energy of proton reduction. This shows that the photocatalytic activity of the nanocrystals depends on the electrochemical potentials/Fermi energies of the modified catalysts. The effect of the PDI charge on the nanomaterial energetics can be rationalized by considering the surface potential. The latter can be related to the particle surface charge and the concentration of counterions in solution using the Grahame equation. These results provide a quantitative basis for the understanding and manipulation of nanomaterial photocatalysts with PDIs.

Received 6th September 2013
Accepted 26th November 2013

DOI: 10.1039/c3ee42993h

www.rsc.org/ees

Broader context

Photoelectrochemical processes at solid–liquid interfaces are at the heart of solar energy conversion technology. Here we show that specifically adsorbed ions (Sr^{2+}, K^+, and H^+) can modify the charge, surface potential, electrochemical potential and photocatalytic proton reduction rate of suspended metal oxide ($HCa_2Nb_3O_{10}$) nanocrystals. The optimization of the photocatalytic proton reduction activity of nanoscale catalysts is central to the generation of hydrogen fuel from water *via* the photocatalytic water splitting reaction. We confirm ion induced charging with zeta potential measurements and measure the corresponding change in the Fermi energy of the nanocrystals with photoelectrochemical methods. The connection between the charge concentration on the nanocrystals and the surface potential change can be understood with the Grahame equation. The observed trend of the photocatalytic hydrogen evolution rate *versus* the Fermi energy can be modelled with a linear free energy relationship. The work opens new ways for the systematic manipulation of nanocrystal photocatalysts with specifically absorbed ions, employing concepts discovered by A. Frumkin over 80 years ago.

Introduction

Photocatalytic water splitting is conceptually the simplest way by which to convert renewable energy from sunlight into hydrogen fuel.[1–5] Metal oxide semiconductors of abundant elements are particularly interesting as water-splitting catalysis due to their higher stability against anodic photocorrosion. Nanoscaling can improve the efficiency of a photocatalyst by increasing surface area and the number of catalytic sites for water-splitting and by reducing the diffusion lengths for charge carriers to reach the surface.[6] Indeed, for many metal oxides and chalcogenides, nanoscaling has resulted in gains in photoelectrochemical activity.[7–13] Ultimately, the activity of photocatalysts is limited by the energetics of the material and by the steady state concentrations of charge carriers that can be achieved under illumination. For overall water splitting, the free energy of the charge carriers (sum of Fermi energies for electrons E_{Fn} and holes E_{Fh}) must exceed the free energy of

Department of Chemistry, University of California, Davis, One Shields Avenue, Davis, CA 95616, USA. E-mail: fosterloh@ucdavis.edu; Fax: +1 5307528995

† Electronic supplementary information (ESI) available: Electron microprobe analyses, charge density calculations, photocurrent scans, and hydrogen evolution data. See DOI: 10.1039/c3ee42993h

formation of water.[14] As we demonstrated recently, the Fermi energies E_{Fn} and E_{Fh} of CdSe nanocrystals can be modified through the quantum size effect, allowing tuning of the photocatalytic proton reduction rate.[15–18] Alternatively, a shift of the Fermi energy of the system can be achieved with specifically-absorbed ions. The effect of these adsorbed, or potential determining ions (PDIs) on the energetics of semiconductor photoelectrodes is well known.[19,20] PDIs affect the redox stability of minerals,[21] and the charge transfer kinetics of many photocatalysts. In water, the flatband potentials of metal oxides, including TiO_2 (ref. 22) and Fe_2O_3 (ref. 23 and 24) are primarily controlled by proton/hydroxide adsorption, and consequently, are linear functions of the solution pH.[21] But other ions, such as phosphate, silicate and fluoride also show strong effects of the surface potential.[25] In contrast, the flatband potentials of II/VI, III/V, and group IV semiconductors are more susceptible to adsorption of soft ions, including sulfide,[26] HS^-,[27,28] HTe^-,[29,30] and Cl^-.[31] Specific ion adsorption has been proposed as cause for unusually large open circuit voltage of (Mo, W)Se_2/NaI_3, GaAs/K_2Se, Cd(S, Se)/Na_2S photoelectrochemical cells.[31] Adsorption of PDIs can also be selective to specific surfaces, *e.g.* in Cd(Se, Te)/HS-, HTe^- the strongest flatband shifts occur for the Cd^{2+} rich (111) surface planes.[29,30]

Theoretically, the effect of specifically adsorbed ions can be understood using the definition of the Fermi energy of the electrons E_F in a particle, which is equal to the chemical potential μ minus the electrical potential ϕ of the material (F: Faraday constant).[32]

$$E_F = \mu - \phi F \quad (1)$$

Adsorbed ions can affect E_F by either changing μ or by changing ϕ, or both. In the literature, proton adsorption is usually considered as an effect on chemical potential μ. For example, if pH_{pzc} is the negative logarithm of the surface proton concentration of the suspended particle at the point of zero charge (pzc or isoelectric point), and pH the negative logarithm of the actual surface proton concentration, the pH-dependent shift of the chemical potential is frequently stated with eqn (2).

$$\Delta\mu = 2.303RT(pH_{pzc} - pH) \quad (2)$$

Indeed, this Nernstian dependence of the semiconductor flatband potential on solution pH and the associated 59 mV shift per pH unit has been experimentally confirmed for many metal oxides.[21–23] And values of pH_{pzc} have been tabulated for many materials.[33–35] Eqn (2) works because redox reactions with protons are usually fast, allowing the protons to be in thermodynamic equilibrium with the electrons in the particle.

But this approach is not suitable for specifically adsorbed cations, which in aqueous solution do not readily participate in redox reactions, because their reduction potentials are too negative. Examples include Al^{3+} (−1.66 V *vs.* NHE) and Mg^{2+} (−2.37 V *vs.* NHE).[36] For these specifically adsorbed ions, an electrostatic approach is more suitable. Here it is assumed that adsorption of the ion generates the charge density $\sigma = q/A$ on the particle of surface area A, which modifies the surface potential ϕ_0 (Fig. 1). If space charge layer effects can be neglected, as is the case for nanoparticles, the potential ϕ felt inside the particle will be the same as ϕ_0, causing E_F to change according to eqn (1). The relation between the surface charge density σ on the particle and the resulting surface potential ϕ_0 is given by the Grahame equation (for definition of constants see ESI†).[37,38]

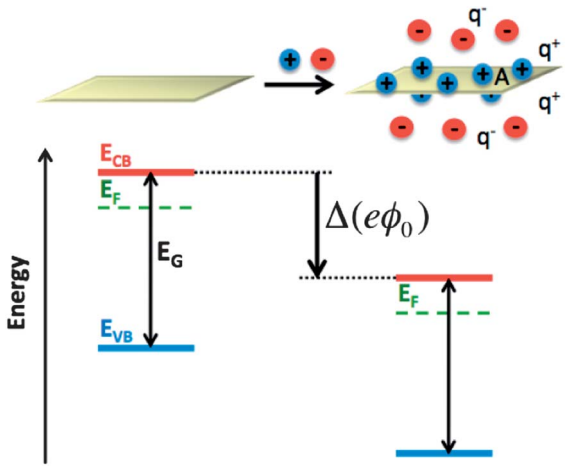

Fig. 1 Energy diagram showing how addition of specifically adsorbed ion affects the energetics of the system.

$$\phi_0 = \frac{2RT}{zF}\sinh^{-1}\left(\frac{\sigma}{\sqrt{8RT\varepsilon\varepsilon_0 c^0}}\right) \quad (3)$$

Here, z and c^0 describe the charge and molar concentration of the *counterions* in solution, which surround the particle. Specifically adsorbed cations will produce a positive surface potential, shifting the energy bands down to more oxidizing potentials, and anions will move the band edges to more reducing potentials.

The corresponding Fermi energy shift predicted by eqn (2) will affect the electron transfer rates to a redox couple in solution. For metal electrodes this *Frumkin* effect was discovered over 80 years ago.[39] In general, the variation of the electron transfer rate constant with E_F can be understood using free energy relationships,[40] including Butler Volmer[41,42] and Marcus theory.[43]

Even though the effects of specifically adsorbed ions on the reactivity of nanomaterials have been noted in the literature,[17,44,45] a quantitative analysis has not been performed. Here, we undertake an attempt to measure the effect of PDIs on the energetics and photocatalytic proton reduction rate with nanocrystals. We choose tetrabutylammonium (TBA) supported $TBA_xH_{1-x}[Ca_2Nb_3O_{10}]$ nanosheets as test material. The nanosheets can be obtained by chemical exfoliation of the layered $KCa_2Nb_3O_{10}$ parent phase.[46] They have lateral dimensions of 100–1000 nm, depending on preparation conditions, but their thickness is fixed at 1.0 nm due to the laminar structure of the sheets (Fig. 2 and 3A), each of which is a single crystal. Under ultraviolet irradiation, suspensions of the nanosheets (E_G = 3.5 eV) have been previously shown to split pure water into hydrogen and hydrogen peroxide[47,48] and to evolve hydrogen

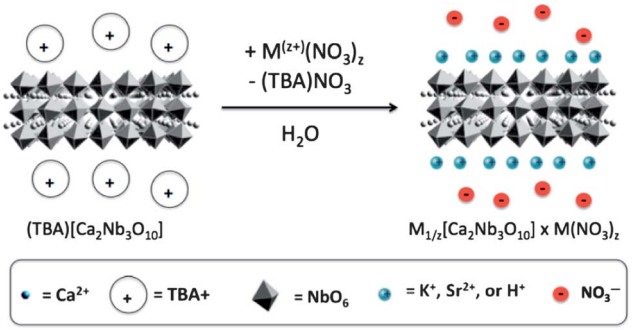

Fig. 2 Modification of $TBA_xH_{1-x}[Ca_2Nb_3O_{10}]$ nanosheets with metal salts.

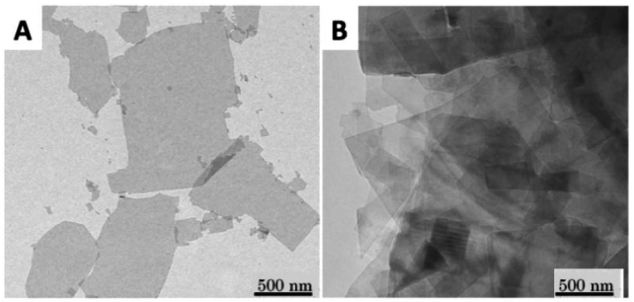

Fig. 3 Transmission electron micrograph (TEM) of (A) $TBA_xH_{1-x}[Ca_2Nb_3O_{10}]$ nanosheets and (B) $Sr_xH_{1-2x}[Ca_2Nb_3O_{10}]$ nanosheets.

from aqueous methanol at rates 30 times higher than bulk $KCa_2Nb_3O_{10}$.[49,50] In neutral water the nanosheets are negatively charged (their point of zero charge, pH_{pzc}, is ~2.5) (ref. 51) and modification with metal cations and protons can be readily achieved through simple mixing with metal salts or acids. Potassium and strontium ions were chosen as modifiers, because these metal cations are non-catalytic for the hydrogen evolution reaction. As we will show in the following, these modifications affect the electrostatic, electronic, and charge transfer properties of the nanomaterial, allowing tuning of the photocatalytic proton reduction and charge transfer activity. These findings should be applicable to other nanoparticles, and thus will likely have a general impact on solar energy conversion and the chemistry of nanomaterials.

Results

Potential determining ion (PDI)-modified nanosheet samples were obtained as shown in Fig. 2, by either mixing a tetrabutylammonium (TBA) stabilized $H_{1-x}[Ca_2Nb_3O_{10}]$ sol with a diluted metal nitrate (K, Sr) solution or by adding dilute hydrochloric acid to the nanosheet sol to achieve a final pH of 1, 3 or 7. During the reaction the loosely bonded TBA cations are displaced by the smaller ions, leading to precipitation of the PDI-modified nanocrystals as a white solid. According to TEM, the solid contains the nanosheets in aggregated form (Fig. 3). The cations are bonded in between these sheets and on their surfaces, similar to the distribution of ions in the Dion Jacobsen

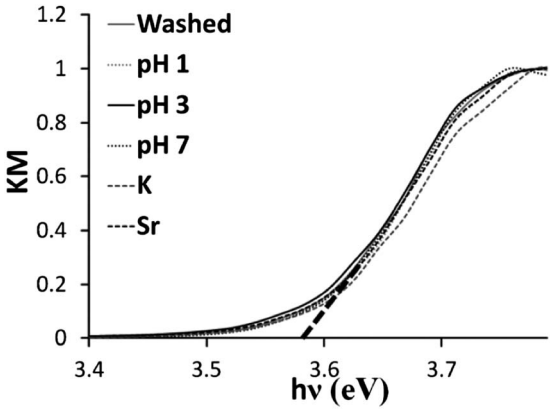

Fig. 4 Diffuse reflectance spectra of films of modified nanosheets.

parent phases $MCa_2Nb_3O_{10}$ (M = H, K).[52–54] According to electron microprobe analysis (data and calculations in ESI†) the precipitated nanosheets contain 0.11 Sr^{2+} and 0.21 K^+ ions per $Ca_2Nb_3O_{10}$ formula unit, with the rest made up by residual TBA ions. Diffuse reflectance spectra (Fig. 4) observe the optical band gap at 3.59 ± 0.05 eV for all samples, which corresponds well with the literature value of 3.53 eV.[47] This data shows that ion modification does not change the band gap of these materials, as expected from the ionic interaction type between cations and the Nb–Ca–O nanosheet body.

Because of eqn (1)–(3), the adsorption of ions to the nanosheets is expected to modify the surface potential. To confirm this, zeta potential ϕ_z titrations were carried out on these samples (Fig. 5) by adding dilute acid. The zeta potential is defined as the surface potential felt by a test charge at the shear plane between the stationary and mobile sections of the electric double layer. The curve for $TBACa_2Nb_3O_{10}$ shows a pH_{pzc} of 2.5, similar to the published value.[51] At pH = 7, the sheets have ϕ_z = −40 mV, in agreement with a negative surface charge of the $Ca_2Nb_3O_{10}^-$ anion. At pH = 3, ϕ_z = 0 mV, due to protonation of the sheets. The titration curve for the K^+-modified sample is shifted to more negative ϕ_z values, *i.e.* the K^+-modified samples are more anionic than the unmodified sheets. Likely the larger

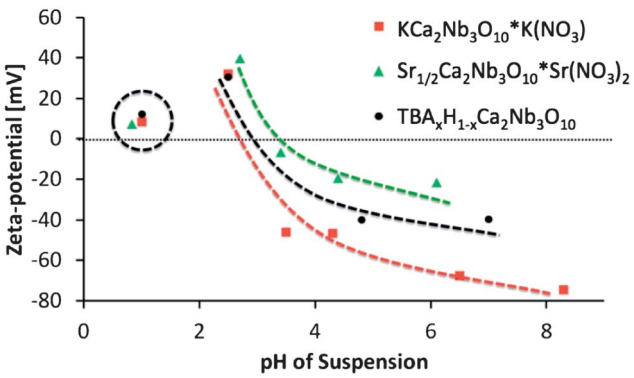

Fig. 5 Zeta potential of nanosheets as a function of the pH (titrated with HCl) of the suspension. The circled values near pH = 1 are due to aggregation of the sheets due to the higher ionic strength of the sample solution, and are excluded from the analysis.

potassium ions block multiple O^{2-} sites from protonation. For the Sr^{2+} modified sample, a shift to more positive ϕ_z values is observed over almost the entire pH range, which is probably a consequence of the double positive charge of the Sr^{2+} ions. Interestingly, the metal ions only have a weak effect on the pH_{pzc} of the samples. These results show that above $[H^+] = 10^{-4}$ M, protons remain the most prominent potential determining ions in this system.

In order to evaluate the effect of PDIs on the Fermi energy, photoelectrochemical scans were conducted on thin films of the nanosheets on FTO coated glass. Anhydrous methanol with 0.1 M TEACl as electrolyte was chosen to minimize secondary protonation/deprotonation of the nanosheets. Tetraalkylammonium chlorides are generally regarded as weakly adsorbing to metal oxides. In the absence of large kinetic barriers for electron transfer, the photoonset potential E_{Ph} is a good approximation of the quasi-Fermi energy, E_{Fn} in illuminated semiconductors.[42,55–59] A typical voltammogram recorded under chopped illumination is shown in Fig. 6A (for remaining data see Fig. S2–4 in ESI†). The scan shows a dark cathodic current stemming from proton reduction at negative applied potentials <−0.6 *vs.* NHE.

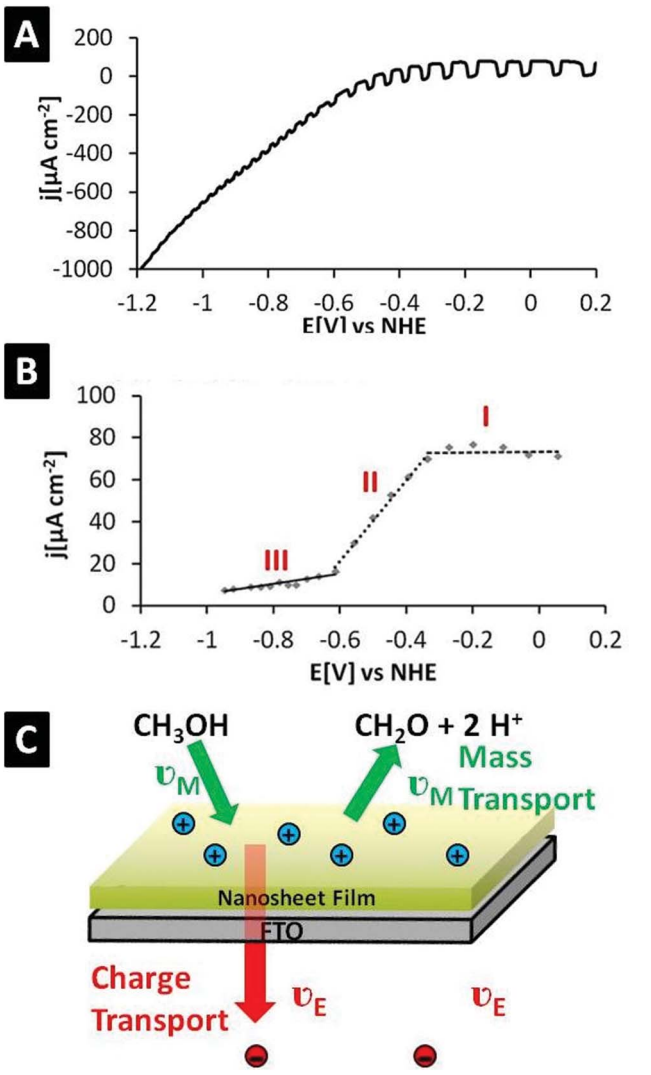

Fig. 6 (A) Photocurrent scan (anodic direction) for pH 7-modified nanosheet film on FTO in methanol with 0.1 M TEACl and using chopped light from a Xe-lamp. (B) Photocurrent density *versus* voltage curve. (C) Limiting charge and mass transfer processes in illuminated nanosheet films. ν_E, diffusion limited current density, ν_M, diffusion limited mass transport flux.

The anodic photocurrent reaches up to 80 μA cm^{-2} and decreases monotonically in cathodic direction. No clear photoonset can be discerned due to the presence of a weak residual photocurrent of approximately 5 μA cm^{-2}. To aid the interpretation of the data, the net photocurrent values were plotted in Fig. 6B as a function of the applied potential. Three potential ranges are apparent in the diagram: a voltage-independent photocurrent at oxidizing potentials (I), a voltage-dependent photocurrent at intermediate potentials (II), and a small voltage-independent residual current at reducing potentials (III). This behavior can be understood using the scheme in Fig. 6C. In region I, the photocurrent is limited by mass transfer (ν_M) at the film–electrolyte interface. In the absence of water, this current is expected to be limited by proton transport. In region II, the photocurrent is controlled by the rate of electron transfer (ν_E), which is dependent on the difference between the Fermi energy of the nanosheet and the applied potential ($E_F - E_{app}$). In region III, the photocurrent densities are very small and show a decreased dependence on the applied bias. As this residual current was not observed in bare FTO substrates, it likely originates from minority states (edge and corner sites) in the nanosheet film and is not diagnostic of the nanosheet energetics. Thus, region II was used to determine the onset potentials by linear extrapolation of trendline to the *x*-axis. The approximated E_{Fn} potentials for all samples are listed in Table 1. Among proton-modified samples, E_{Fn} values decrease in the expected order from −0.62 V for the proton rich sample to −0.71 V for the proton poor sample. This trend is similar to that seen for the zeta potentials in Fig. 5, where increasing protonation moves the surface potential to more positive values. Values for metal-ion modified samples are −0.59 V for the Sr^{2+} modified sample and −0.67 V for the K^+ modified sample. These results show that the metal cations move the quasi Fermi level of non-modified (pH = 7) sheets to more oxidizing potentials, as expected. The divalent cation is more efficient because of the higher positive charge, compared to potassium ion.

The observed variations of E_{Fn} values resulting from specific adsorption of cations correspond well to the electrostatic model in eqn (1) and (3). If the change in E_{Fn} = +0.12 eV upon Sr^{2+} adsorption (E_{Fn} = −0.59 V from −0.71 V for TBA nanosheets at pH = 7) is solely due to the alteration of nanosheet surface potential according to eqn (1), the surface cation density can be estimated with the Grahame equation (eqn (3), calculation details in ESI†). Using $\varepsilon = 30$ for methanol, $T = 298$ K, $c^0 = 0.01 \times 10^3$ mol m^{-3} of Cl^- counterions, and a Sr^{2+} ion-induced surface potential of ϕ_0 = +0.12 V, one obtains $\sigma = 0.78$ elemental charges per nanosheet formula unit. This value differs from the electron microprobe data that observes 0.11 Sr^{2+} ions, *i.e.* +0.22 positive charges per $HCa_2Nb_3O_{10}$ formula unit. The difference is due to the unknown degree of

Table 1 Selected data for modified nanosheets

Sample	E_G/eV	E_{Fn}/V *vs.* NHE	$r(H_2)$/μmol h^{-1}/25 mg	ζ/mV	$E_0(H^+/H_2)$/V
H^+ (pH = 1)	3.60	−0.62	160	+12	−0.06
H^+ (pH = 3)	3.58	−0.68	60	0	−0.18
H^+ (pH = 7)	3.59	−0.71	20	−40	−0.41
Sr^{2+}	3.59	−0.59	70 (pH = 1)	+7 (pH = 1), −7 (pH = 3), −20 (pH = 7)	−0.06
K^+	3.59	−0.67	350 (pH = 1)	+8 (pH = 1), +32 (pH = 3), −68 (pH = 7)	−0.06

protonation of the nanosheets during the electrochemical experiment. We also note that the calculation result depends strongly on the unknown Cl^- counterion concentration c^0 in the nanosheet film, which is set at 0.01 M, *i.e.* 10% of solution concentration. The lower chloride concentration in the film is expected on the basis of the limited ability of the $(C_2H_5)_4NCl$ electrolyte to penetrate the film (large tetraethylammonium ion). For the K^+-modified sheets the induced surface potential ϕ_0 = +0.04 V, and the calculation yields σ = 0.131 elemental charges per formula unit, similar to the result of the elemental composition data (0.21 K^+ ions per $Ca_2Nb_3O_{10}$ formula unit).

As mentioned above, the change in E_{Fn} values is expected to modify the charge transfer kinetics of the nanosheet photocatalysts. To test this hypothesis, photocatalytic hydrogen evolution experiments were performed with 25 mg of the suspended nanosheet samples in aqueous methanol (Fig. 7 and Table 1). For proton-modified nanosheets, the pH of the solution during irradiation had to appropriately correspond with the pH of the H^+ modified samples. Therefore, these samples were irradiated at pH = 1, 3, 7 *via* addition of 0.1 M HCl. In all cases, linear hydrogen evolution was observed without apparent initial activation period or decay at the end of the experiments. Rates (20–350 μmol H_2 h^{-1}) were low and appeared limited by the absence of a proton reduction cocatalyst.[7,60,61] Platination of the samples was avoided to rule out interference with adsorption of Pt^{2+} cations. The potassium modified phase $K_xH_{1-x}[Ca_2Nb_3O_{10}]$ is the most active for water reduction and pH 7-$H_x[Ca_2Nb_3O_{10}]$ is the least active. Successive irradiation experiments at later times confirmed these relative activity differences, although a trend of decreasing photocatalytic activity with aging of the stock $TBA_xH_{1-x}[Ca_2Nb_3O_{10}]$ was also observed (Fig. S5†). The reason for the decay in activity with aging time is not clear.

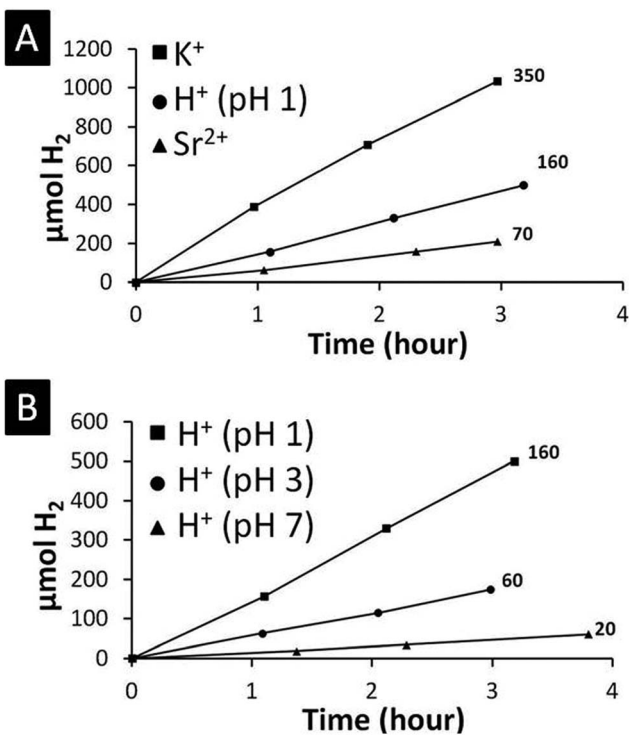

Fig. 7 (A) Hydrogen evolution from Sr/K/H-modified nanosheets at pH 1 (adjusted with HCl) and (B) H_2 evolution from H-modified nanosheets at pH 1, 3, 7 (adjusted with HCl). Results are for 25 mg of catalyst dispersed in 50 mL 20% (vol) aqueous methanol in 100 mL quartz flask under irradiation from 300 W Xe arc lamp (1 W cm^{-2} at flask surface). Labels indicate evolution rates per hour.

In Fig. 8A the measured proton reduction rates are plotted against the free energy of proton reduction, as given by the difference of quasi-Fermi Energy and proton reduction potential ($\Delta G = E_{Fn} - FE(H^+/H_2)$). As the free energy of proton reduction increases, due to the change in E_{Fn} or the proton reduction potential, an exponential rise in activity is observed. The reason for this trend can be understood on the basis of the energy scheme for the photocatalytic water reduction system (Fig. 7B). Because the proton reduction potential is quite close to the Fermi energy of the electrons, the driving force for proton reduction is small, and even small variations of E_{Fn} or $E(H^+/H_2)$ will affect it. On the other hand, methanol oxidation occurs through holes in the strongly oxidizing valence band. This driving force is large and *relatively* independent of pH and potential determining ions. This makes proton reduction, not methanol oxidation, the rate-limiting step.

The data in Fig. 8A can be fitted with the linear free energy relationship (LFER) in eqn (4),[40] with F = 96485 C mol^{-1}, R = 8.314 J mol^{-1} K^{-1}, T = 298 K, A = 0.0127, α = 0.441, and β = 633 J mol^{-1}.

$$R = A \exp\left[-\frac{\alpha F(E_{Fn} - FE) + \beta}{RT}\right] \quad (4)$$

Here, the $(E_{Fn} - FE)$ term in the equation is the thermodynamic driving force for proton reduction. Values range between −29.0 and −58.9 kJ mol^{-1}, depending on PDI modification and solution pH. In the present format of eqn (4), the numerical values of α and β do not have physical significance, because the fitted rate R [μmol h^{-1}] does not convey any information about the value of the rate constant for the process, which depends on the electro-active area of the nanoparticles, the absorbed

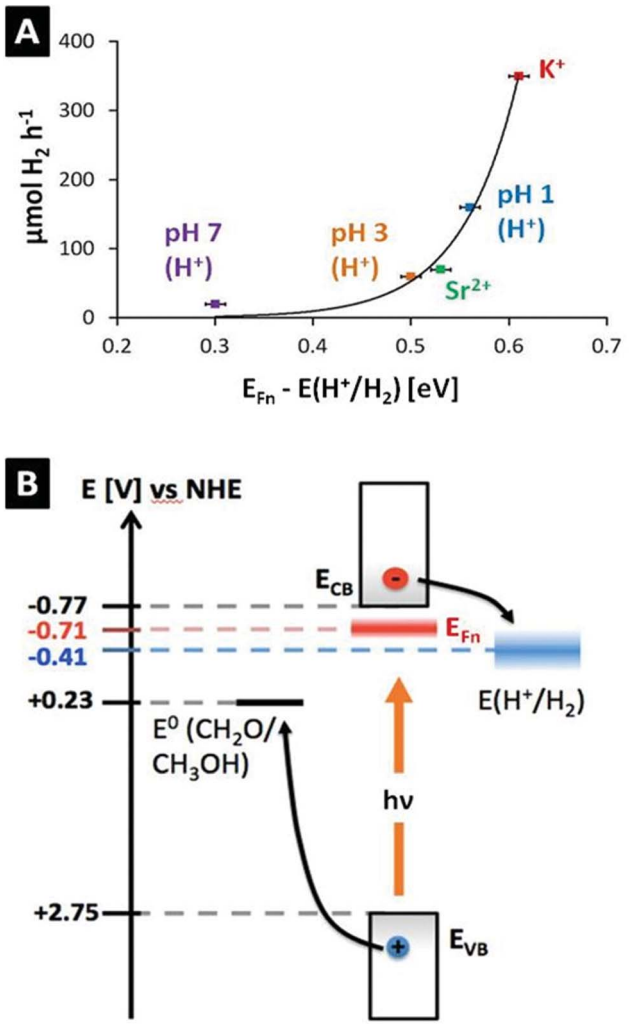

Fig. 8 (A) Calculated rate of hydrogen evolution *versus* ΔG for electron transfer. For data see Table 1. (B) Energy scheme for photocatalytic proton reduction at pH = 7. The methanol oxidation potential is from ref. 68.

photons flux, space charge layer effects, and other unknown parameters.[62–67] Nevertheless, eqn (4) provides a simple physical explanation for the observed correlation between nanosheet energetics and hydrogen evolution rates. Furthermore, it confirms the dependence of photocatalytic activity on the presence of specifically adsorbed ions.

Conclusions

In summary, we have demonstrated that modification of $TBA_xH_{1-x}[Ca_2Nb_3O_{10}]$ nanosheets with specifically adsorbed K^+, Sr^{2+}, and H^+ ions leads to altered electrostatic, energetic and photocatalytic properties of this nanomaterial. The modifications were quantitatively analyzed with zeta potential and photoelectrochemical and photocatalytic measurements, and modeled with the Grahame equation and a linear free energy relationship. The ability to adjust energetics and charge transfer properties of nanomaterials is central to their use in advanced solar energy conversion technology, and to the understanding of their redox properties. The concepts described here should be applicable to other nanomaterials.

Experimental

K_2CO_3, $CaCO_3$, Nb_2O_5, and TBA(OH) (40 wt% in H_2O) were purchased from Acros Organics, Morris Plains, NJ. KNO_3 (99.0%), $Sr(NO_3)_2$ (99.9%), methanol (99.9%), and HCl (37.3% purity) were purchased from Fisher Scientific. Tetraethylammonium chloride (TEACl, 98%) was purchased from Eastman Kodak. F:SnO_2 (FTO) (TEC 15) on glass substrates were purchased from MTI Corporation. Water was purified by a Nanopure II system to a resistivity of >18 MΩ cm. Solutions were bubbled with high purity nitrogen gas (99.9% purity) to remove residual oxygen. TBA_xH_{1-x} $[Ca_2Nb_3O_{10}]$ nanosheets were synthesized as reported before and stored in aqueous TBA(OH) at a pH of 11.[69,70]

K, Sr-modified $Ca_2Nb_3O_{10}$

A portion of the stock solution of $TBA[Ca_2Nb_3O_{10}]$ was washed with water and centrifuged repeatedly until the wash solution was pH 9. Then 2.0 mL of the sol (~6 w/w%) were mixed with 40 mL of a degassed solution of 1.0 M aqueous KNO_3 or $Sr(NO_3)_2$ for 1 hour. The mixture was washed and centrifuged 3 times to remove excess metal cations and nitrate before storing the precipitate in ultrapure water.

pH-modified $Ca_2Nb_3O_{10}$

A 2.0 mL portion of the stock solution of $TBA[Ca_2Nb_3O_{10}]$ was washed to pH 9 and the pH was further adjusted with dilute HCl to pH 1, 3, or 7 before irradiation. Catalyst amounts were determined by gravimetric analysis.

Electrochemistry

Photoelectrochemical measurements were performed using a three-electrode cell equipped with a Pt counterelectrode and a Ag/AgCl reference electrode, containing 1.0 M TEACl in methanol. A fluorine-doped tin oxide (FTO) coated glass electrode (1.0 cm^2 exposed area) served as the working electrode. Suspensions of the modified nanosheets were drop-cast on the FTO electrodes and dried at 200 °C for 30 minutes. The cell electrolyte consisted of 0.1 M TEACl in non-aqueous methanol. Water was excluded to avoid hydroxide/protons as potential determining ions. The solutions were degassed with N_2 for ten minutes prior to each measurement. The potential of the $K_4[Fe(CN)_6]$ redox couple was used to calibrate each measurement. Potentials were generated and currents observed with a Gamry Reference 600 potentiostat controlled by a PC. Photocurrent onset potentials were measured by applying cathodic scans (10 mV s^{-1}) with chopped light from a 300 W Xe arc lamp, filtered with a water IR filter, and directed onto the working electrode using SiO_2 fiber optics. The power at the electrode was 20 ± 5 mW cm^{-2} as determined with a GaAsP photodetector (280 nm to 660 nm sensitivity range). Based on 3–4 repeated scans, the error for photoonset potentials is ±0.01 V.

Irradiation and H_2 measurement

Solutions of the modified catalysts were irradiated with a 300 W Xe arc lamp equipped with an IR water filter. The light intensity at the center of the flask was 700 mW cm^{-2}, as measured with a GaAsP detector. The gas samples were analyzed with a Varian 3800 gas chromatograph using Ar carrier gas, a Supelco 60/80 molecular sieve 5 Å column, and a thermal conductivity detector. Solutions were prepared with 25 mg of the modified catalyst dispersed in 50 mL 20% aqueous methanol in a 100 mL quartz flask and adjusted to pH 1, 3, or 7 with 0.005 M to 0.1 M HCl. Sr- and K-modified samples gave less reproducible data at pH = 7, hence these measurements were done at pH = 1. The temperature of each solution was initially 25 °C and reached a maximum of 35 °C after irradiation. Each solution was initially degassed with three cycles of vacuum evacuation and Ar fill to 600 Torr. Gas samples were periodically removed from the headspace *via* a closed loop injection system.

Other measurements

Diffuse reflectance UV-vis spectra were collected using a Thermo Scientific Evolution 220 UV-Vis Spectrophotometer equipped with an integrating sphere. Transmission electron microscopy (TEM) images were gathered using a Philips CM120 transmission electron microscope and a Gatan MegaScan digital camera. TEM samples were prepared by drop-casting a dilute solution of each sample onto holey carbon-coated Cu grids. Centrifugation was performed with a Fisher Scientific Marathon 21000 centrifuge at 13750 rpm. Zeta-potential measurements were obtained with a Malvern Nano ZS90 Zetasizer at 298 K on aqueous nanocrystal sols (~0.5 mass %) that were titrated with 0.005 M to 0.1 M HCl.

Acknowledgements

FEO thanks Research Corporation for Science Advancement for a Scialog award. This work was further supported by the National Science Foundation (NSF, grants 1152250 and 1133099). RLC thanks Dr Min Wang and Prof. Nitin Nitin for Zetasizer instrument training and access and Nick Botto and Sarah Roeske in the UCD Geology department for electron microprobe analyses.

References

1 A. Kudo and Y. Miseki, *Chem. Soc. Rev.*, 2009, **38**, 253–278.
2 F. E. Osterloh, *Chem. Mater.*, 2007, **20**, 35–54.
3 R. Krol, *Principles of Photoelectrochemical Cells*, Springer US, 2012.
4 M. G. Walter, E. L. Warren, J. R. McKone, S. W. Boettcher, Q. X. Mi, E. A. Santori and N. S. Lewis, *Chem. Rev.*, 2010, **110**, 6446–6473.
5 M. B. Wilker, K. J. Schnitzenbaumer and G. Dukovic, *Isr. J. Chem.*, 2012, **52**, 1002–1015.
6 F. E. Osterloh, *Chem. Soc. Rev.*, 2013, **42**, 2294–2320.
7 T. K. Townsend, E. M. Sabio, N. D. Browning and F. E. Osterloh, *ChemSusChem*, 2011, **4**, 185–190.
8 M. C. Sarahan, E. C. Carroll, M. Allen, D. S. Larsen, N. D. Browning and F. E. Osterloh, *J. Solid State Chem.*, 2008, **181**, 1678–1683.
9 F. A. Frame, T. K. Townsend, R. L. Chamousis, E. M. Sabio, T. Dittrich, N. D. Browning and F. E. Osterloh, *J. Am. Chem. Soc.*, 2011, **133**, 7264–7267.
10 H. Kato, K. Asakura and A. Kudo, *J. Am. Chem. Soc.*, 2003, **125**, 3082–3089.
11 A. Kay, I. Cesar and M. Grätzel, *J. Am. Chem. Soc.*, 2006, **128**, 15714–15721.
12 T. K. Townsend, N. D. Browning and F. E. Osterloh, *ACS Nano*, 2012, **6**, 7420–7426.
13 K. Maeda and K. Domen, *J. Phys. Chem. Lett.*, 2010, **1**, 2655–2661.
14 A. Kumar, P. G. Santangelo and N. S. Lewis, *J. Phys. Chem*, 1992, **96**, 834–842.
15 J. Zhao, M. A. Holmes and F. E. Osterloh, *ACS Nano*, 2013, **7**, 4316–4325.
16 M. A. Holmes, T. K. Townsend and F. E. Osterloh, *Chem. Commun.*, 2012, **48**, 371–373.
17 F. A. Frame and F. E. Osterloh, *J. Phys. Chem. C*, 2010, **114**, 10628–10633.
18 F. Andrew Frame, E. C. Carroll, D. S. Larsen, M. Sarahan, N. D. Browning and F. E. Osterloh, *Chem. Commun.*, 2008, 2206–2208.
19 M. A. a. G. Butler and D. S. Ginley, *J. Electrochem. Soc.*, 1978, **125**, 228–232.
20 P. Singh, R. Singh, R. Gale, K. Rajeshwar and J. DuBow, *J. Appl. Phys.*, 1980, **51**, 6286–6291.
21 G. E. Brown, V. E. Henrich, W. H. Casey, D. L. Clark, C. Eggleston, A. Felmy, D. W. Goodman, M. Gratzel, G. Maciel, M. I. McCarthy, K. H. Nealson, D. A. Sverjensky, M. F. Toney and J. M. Zachara, *Chem. Rev.*, 1999, **99**, 77–174.
22 L. Kavan, M. Gratzel, S. E. Gilbert, C. Klemenz and H. J. Scheel, *J. Am. Chem. Soc.*, 1996, **118**, 6716–6723.
23 S. U. M. Khan and J. Akikusa, *J. Phys. Chem. B*, 1999, **103**, 7184–7189.
24 R. J. Atkinson, A. M. Posner and J. P. Quirk, *J. Phys. Chem.*, 1967, **71**, 550–558.
25 F. J. Hingston, R. J. Atkinson, A. M. Posner and J. P. Quirk, *Nature*, 1967, **215**, 1459–1461.
26 D. Meissner, R. Memming and B. Kastening, *J. Phys. Chem.*, 1988, **92**, 3476–3483.
27 D. S. Ginley and M. A. Butler, *J. Electrochem. Soc.*, 1978, **125**, 1968–1974.
28 K. W. Frese and D. G. Canfield, *J. Electrochem. Soc.*, 1984, **131**, 2614–2618.
29 D. Lincot and J. Vedel, *J. Phys. Chem.*, 1988, **92**, 4103–4110.
30 H. Minoura, T. Watanabe, T. Oki and M. Tsuiki, *Jpn. J. Appl. Phys.*, 1977, **16**, 865–866.
31 P. Singh, R. Singh, R. Gale, K. Rajeshwar and J. Dubow, *J. Appl. Phys.*, 1980, **51**, 6286–6291.
32 A. J. Bard and L. R. Faulkner, *Electrochemical methods: fundamentals and applications*, John Wiley, New York, 2001.
33 M. Kosmulski, *Adv. Colloid Interface Sci.*, 2009, **152**, 14–25.
34 M. Kosmulski, *J. Colloid Interface Sci.*, 2011, **353**, 1–15.
35 M. Kosmulski, *J. Colloid Interface Sci.*, 2002, **253**, 77–87.

36 P. Vanysek, in *CRC Handbook of Chemistry and Physics*, CRC Press/Taylor and Francis, Boca Raton, FL, 88 (Internet Version 2008) edn., 2008.
37 A. J. Bard and L. R. Faulkner, *Electrochemical methods: fundamentals and applications*, John Wiley, New York, 2001.
38 D. C. Grahame, *Chem. Rev.*, 1947, **41**, 441–501.
39 A. J. Bard and L. R. Faulkner, *Electrochemical methods: fundamentals and applications*, John Wiley, New York, 2001.
40 J. M. Mayer, *Annu. Rev. Phys. Chem.*, 2004, **55**, 363–390.
41 A. J. Bard and L. R. Faulkner, *Electrochemical methods: fundamentals and applications*, John Wiley, New York, 2001.
42 J. Zhao, M. A. Holmes and F. E. Osterloh, *ACS Nano*, 2013, **7**, 4316–4325.
43 R. A. Marcus, *Annu. Rev. Phys. Chem.*, 1964, **15**, 155–196.
44 L. M. Peter, K. G. U. Wijayantha, D. J. Riley and J. P. Waggett, *J. Phys. Chem. B*, 2003, **107**, 8378–8381.
45 V. Chakrapani, K. Tvrdy and P. V. Kamat, *J. Am. Chem. Soc.*, 2010, **132**, 1228–1229.
46 M. M. J. Treacy, S. B. Rice, A. J. Jacobson and J. T. Lewandowski, *Chem. Mater.*, 1990, **2**, 279–286.
47 O. C. Compton, E. C. Carroll, J. Y. Kim, D. S. Larsen and F. E. Osterloh, *J. Phys. Chem. C*, 2007, **111**, 14589–14592.
48 O. C. Compton and F. E. Osterloh, *J. Phys. Chem. C*, 2008, **113**, 479–485.
49 E. M. Sabio, R. L. Chamousis, N. D. Browning and F. E. Osterloh, *J. Phys. Chem. C*, 2012, **116**, 3161–3170.
50 E. M. Sabio, R. L. Chamousis, N. D. Browning and F. E. Osterloh, *J. Phys. Chem. C*, 2012, **116**, 19051.
51 K. Maeda, M. Eguchi, S.-H. A. Lee, W. J. Youngblood, H. Hata and T. E. Mallouk, *J. Phys. Chem. C*, 2009, **113**, 7962–7969.
52 M. Dion, M. Ganne and M. Tournoux, *Mater. Res. Bull.*, 1981, **16**, 1429–1435.
53 A. J. Jacobson, J. T. Lewandowski and J. W. Johnson, *J. Less-Common Met.*, 1986, **116**, 137–146.
54 K. Domen, J. Yoshimura, T. Sekine, A. Tanaka and T. Onishi, *Catal. Lett.*, 1990, **4**, 339–343.
55 M. Waller, T. K. Townsend, J. Zhao, E. M. Sabio, R. L. Chamousis, N. D. Browning and F. E. Osterloh, *Chem. Mater.*, 2012, **24**, 698–704.
56 T. K. Townsend, N. D. Browning and F. E. Osterloh, *ACS Nano*, 2012, **6**, 7420–7426.
57 H. R. Sprunken, R. Schumacher and R. N. Schindler, *Faraday Discuss.*, 1980, **70**, 55–66.
58 G. C. Chen, J. M. Zen, F. R. F. Fan and A. J. Bard, *J. Phys. Chem.*, 1991, **95**, 3682–3687.
59 M. A. Butler, *J. Appl. Phys.*, 1977, **48**, 1914–1920.
60 M. C. Sarahan, E. C. Carroll, M. Allen, D. S. Larsen, N. D. Browning and F. E. Osterloh, *J. Solid State Chem.*, 2008, **181**, 1681–1686.
61 O. C. Compton, E. C. Carroll, J. Y. Kim, D. S. Larsen and F. E. Osterloh, *J. Phys. Chem. C*, 2007, **111**, 14589–14592.
62 A. J. Nozik and R. Memming, *J. Phys. Chem.*, 1996, **100**, 13061–13078.
63 R. J. D. Miller and R. Memming, in *Nanostructured and Photoelectrochemical Systems for Solar Photon Conversion*, ed. M. D. Archer and A. J. Nozik, Imperial College Press, London, 2008, vol. 3.
64 R. Memming, *Electron Transfer I*, 1994, **169**, 105–181.
65 G. Chmiel and H. Gerischer, *J. Phys. Chem.*, 1990, **94**, 1612–1619.
66 B. M. Klahr and T. W. Hamann, *J. Phys. Chem. C*, 2011, **115**, 8393–8399.
67 M. X. Tan, P. E. Laibinis, S. T. Nguyen, J. M. Kesselman, C. E. Stanton and N. S. Lewis, in *Progress in Inorganic Chemistry*, 1994, vol. 41, pp. 21–144.
68 G. T. Burstein, C. J. Barnett, A. R. Kucernak and K. R. Williams, *Catal. Today*, 1997, **38**, 425–437.
69 A. J. Jacobson, J. W. Johnson and J. T. Lewandowski, *Inorg. Chem.*, 1985, **24**, 3727–3729.
70 Y. Ebina, I. Sasaki and A. Watanabe, *Solid State Ionics*, 2002, **151**, 177–182.